Research Article | Vol. 27, No. 4 | 18 Feb 2019 | OPTICS EXPRESS 5097
Optics EXPRESS

Correlation of circular differential optical absorption with geometric chirality in plasmonic meta-atoms

JON C. WILSON,[1] PHILIPP GUTSCHE,[2,3] SVEN HERRMANN,[2] SVEN BURGER,[2] AND KEVIN M. MCPEAK[1,*]

[1]*Department of Chemical Engineering, Louisiana State University, Baton Rouge, LA 70803, USA*
[2]*Zuse Institute Berlin, Berlin, Germany*
[3]*Freie Universität Berlin, Berlin, Germany*
**kmcpeak@lsu.edu*

Abstract: We report a strong correlation between the calculated broadband circular differential optical absorption (CDOA) and the geometric chirality of plasmonic meta-atoms with two-dimensional chirality. We investigate this correlation using three common gold meta-atom geometries: L-shapes, triangles, and nanorod dimers, over a broad range of geometric parameters. We show that this correlation holds for both contiguous plasmonic meta-atoms and non-contiguous structures which support plasmonic coupling effects. A potential application for this correlation is the rapid optimization of plasmonic nanostructure for maximum broadband CDOA.

1. Introduction

Metasurfaces exhibiting circular differential optical absorption (CDOA), defined as the differential absorption of left- or right-handed circularly polarized light (LCPL, RCPL), have broad technological applications in photodetection [1], enantiomeric sensing [2,3], super-resolution imaging [5], and ultra-thin broadband optical components [6]. Chiral plasmonic meta-atoms, those who are not congruent with their mirror image, can display CDOA due to their intrinsic optical activity [7,8]. However, plasmonic meta-atoms with only planar dissymmetry can also exhibit CDOA and asymmetric transmission of CPL through coupling between misaligned plasmon modes [9,10]. These planar structures are commonly labeled as two-dimensionally chiral since they can only be superimposed on their mirror image when lifted from the plane [9]. Two-dimensionally chiral meta-atoms do not exhibit true optical activity due to their perpendicular mirror symmetry [9]. Nonetheless, their non-Minkowski symmetric Mueller matrix [10–12] results in important optical effects such as CDOA and asymmetric transmission (AT), i.e., the differential transmission of forward and backward illumination through a device. Understanding the relationship between the geometry of two-dimensional plasmonic chiral meta-atoms and their resulting broadband CDOA response is important for both understanding plasmonic chiroptical effects [13–17] and optimizing future metasurfaces for integrated photonic and plasmonic all-optical devices [18]. Here we focus on plasmonic structures due to the numerous reports of large planar chiroptical effects [6,9,19,20].

To compare CDOA values between different plasmonic meta-atoms CDOA needs to be normalized by the total absorption in the structure. The normalized CDOA value is commonly referred to as the anisotropic dissymmetry factor, g_{abs}, which is defined as:

$$g_{abs} = \frac{I_L - I_R}{\frac{1}{2}(I_L + I_R)} \tag{1}$$

#349228 https://doi.org/10.1364/OE.27.005097
Journal © 2019 Received 29 Oct 2018; revised 26 Dec 2018; accepted 26 Dec 2018; published 11 Feb 2019

Optics EXPRESS

where I_L and I_R are the absorption intensities for LCPL and RCPL, respectively [21]. Electromagnetic field solvers can calculate g_{abs} for a wide variety of plasmonic meta-atoms but these simulations are resource intensive often requiring high-performance computer clusters to solve when high numerical accuracy is required. A purely geometric based method for predicting trends in g_{abs} for various plasmonic nanostructures could save time and computing resources. Quantifying the chirality of molecules and arbitrary objects solely based on their geometry has a long history starting with Guye introducing the "produit d'asymétrie" [22], the first algebraic function designed to correlate optical rotation with molecular structure [23]. Geometric chirality measures such as the "produit d'asymétrie" are scale invariant since shape, not size, determines the geometric chirality of an object. In general, there are two different classes of geometric chirality measures: the first compare chiral objects to their achiral analog while the second compare the two mirror images of the chiral object to each other [23]. Metrics which fall into the second class are commonly referred to as overlap methods [24,25]. The chiral coefficient, χ, developed by Gilat [26] is an overlap method defined as:

$$\chi = \frac{A_{min}}{2A_{tot}} \tag{2}$$

where A_{min} is the minimum non-overlapping area, i.e., the light grey region in Fig. 1, between a two-dimensionally chiral object (ABCD) and its mirror image (A'B'C'D'), and A_{tot} is the total area of the two-dimensionally chiral object (ABCD). A_{min} is determined by rotating in-plane and translating (A'B'C'D') to achieve maximum overlap with (ABCD). Although overlap methods for computing geometric chirality have existed for many years [26], Potts *et al*. [24] were the first to use such a technique to study the geometric chirality of planar chiral metamaterials. However, direct comparison between geometric chirality and optical properties was only done in passing.

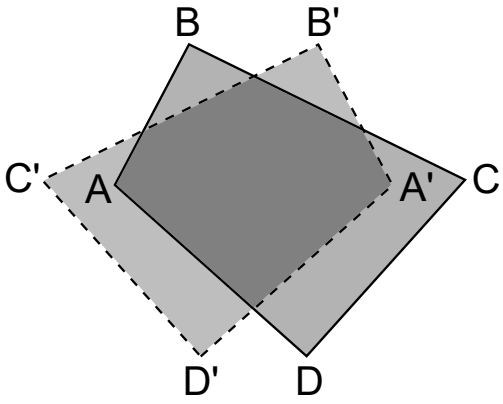

Fig. 1. (ABCD) is a planar chiral object and (A'B'C'D') is its mirror reflection. A_{tot} is the area of (ABCD) and A is the non-overlapping area (light-grey) between (ABCD) and (A'B'C'D'). By varying (A'B'C'D') through any proper translations and/or rotations a minimum non-overlapping area, A_{min} can be found. $\chi = A_{min} / 2A_{tot}$ is the chiral coefficient of (ABCD). Objects with larger values of χ are more geometrically chiral.

Optics EXPRESS

We report a strong correlation between χ and the calculated broadband CDOA for two-dimensionally chiral plasmonic meta-atoms. We introduce the integrated anisotropic dissymmetry factor, $\bar{g}$, as a new metric for broadband CDOA which we define as:

$$\bar{g} = \frac{\int |g_{abs}| d\lambda}{\int d\lambda} \tag{3}$$

where g_{abs} is from Eq. (1), λ is the wavelength and both integrations are over the range of wavelengths where the two-dimensional plasmonic meta-atom absorbs light. The absolute value of the anisotropic dissymmetry factor is used to ensure that both left- and right-handed CDOA contribute to the integrated value. We calculate χ and $\bar{g}$ for isolated two-dimensionally chiral L-shaped, triangular and dimer meta-atoms over a broad range of geometric parameters. We show that for all three geometries there exists a strong correlation between χ and $\bar{g}$. Furthermore, we find the geometric parameters for each of the meta-atoms which maximize χ also maximizes $\bar{g}$. χ is calculated for two-dimensionally chiral objects in seconds on a modern laptop vs. hours or even days to compute $\bar{g}$ over a range of geometries on large-scale, high-performance computers. The rapid computation of χ on low-cost hardware make it a potentially useful tool for rapidly determining the optimum geometric parameters to maximize the broadband CDOA of two-dimensionally chiral plasmonic meta-atoms.

2. Simulations

We calculated the CDOA and total absorption from isolated Au L-shaped, triangular and dimer meta-atoms using JCMsuite, a full-wave finite element Maxwell's equations solver [27]. To provide a realistic model, we rounded the corners of all shapes with 5 to 20 nm radii depending on the size of the meta-atom. We note that our rounding does not break mirror symmetry. Additionally, because no substrate, adhesion layer, or asymmetric rounding/bevel is included, mirror symmetry is still maintained [9]. For the absorbance calculations, all meta-atoms were excited with normal incidence left- and right-circularly polarized plane waves. Calculations were performed every 10 nm over the 400 nm to 1500 nm wavelength range, which captured the primary optical response of the meta-atoms. We calculated the differential and total absorption values for each meta-atom structure as a function of geometric parameters. We then used these absorption values in Eq. (1) to determine the wavelength dependent anisotropic dissymmetry factor, g_{abs}. The definite integral of $|g_{abs}|$ was approximated over the 400 – 1500 nm wavelength range using the composite trapezoidal rule with 10 nm divisions. We divided the result of the numerical integration of $|g_{abs}|$ by the length of the integration interval to generate $\bar{g}$ at specific geometric conditions for each meta-atom.

To better understand the polarization properties of the three meta-atom geometries (L-shape, triangle, and dimer) we calculated their 4 x 4 Mueller matrices **M**. We ran simulations with normal incidence X and Y linearly polarized plane waves to generate the Mueller matrices from the two linearly independent sources. The 16 element Mueller matrix fully describes how a meta-atom alters the polarization state of light [28–30]. Polarization changes can occur through three primary effects, diattenuation—the change in the amplitude for a specific polarization, retardance—the change in phase for a specific polarization, and depolarization—a change in the degree of polarization. A single nanoparticle excited with a plane wave is not able to exhibit depolarization [31], leaving diattenuation and retardance as the possible optical effects. We also verified that each meta-atom geometry was non-depolarizing by calculating their depolarization index as unity [32,33]. Diattenuation and retardance are common optical effects exhibited by anisotropic plasmonic nanostructures [34]. While comparing the

Optics EXPRESS

relationship between elements in the Mueller matrix give us some understanding of the polarization properties of the meta-atoms, we need to relate the Mueller matrix back to the fundamental optical effects of diattenuation and retardance to understand the polarization effects better. The Mueller matrix of homogeneous, non-depolarizing media can be described by seven fundamental parameters using the differential Mueller matrix, **L**, shown in Eq. (4).

$$\boldsymbol{M} = \exp\left(\boldsymbol{L}\right) = \exp\begin{pmatrix} A & -LD & -LD' & CD \\ -LD & A & CB & LB' \\ -LD' & -CB & A & -LB \\ CD & -LB' & LB & A \end{pmatrix} \tag{4}$$

Where A is absorption, LD is linear dichroism at $0°$, LD' is linear dichroism at ± 45°, CD is circular dichroism, LB is linear birefringence at $0°$, LB' is linear birefringence at ± 45°, and CB is circular birefringence. Assuming zero depolarization, we used the analytical inversion method developed by Arteaga *et al.* [4] to calculate the differential Mueller matrix, **L** and determine the polarization effects from each meta-atom and ultimately better understand the origin of their CDOA.

Chiral coefficient values were computed using code developed by the authors [35] in Python. Two-dimensional polygons and their mirror images were generated using the Shapely package. The objective function to be minimized was defined as the non-overlapping area between the two mirror images with rotation and translation as parameters. Optimization was performed using the Scipy differential evolution algorithm with a tolerance of $1x10^{-5}$ and all other parameters as the default. The computed values were normalized by the respective shape areas to get χ.

3. Results and discussion

3.1 L-shaped meta-atoms

Plasmonic L-shaped meta-atoms are an excellent case study for two-dimensionally chiral media. Varying their arm lengths allows facile tuning of their symmetry condition and resulting optical response. Menzel *et al*. reported that L-shaped particles sitting in the x-y plane with equal length arms have mirror symmetry in the x-y plane (M_{xy}) and C_2 symmetry along a diagonal in the x-y plane whereas L-shaped particles with dissimilar arm lengths only exhibited M_{xy} symmetry [36]. Jing *et al*. investigated the even and odd plasmon modes in L-shaped gold nanoparticles and found that only particles with dissimilar arm lengths could excite both even and odd modes [37]. Fig. 2(a) shows a schematic of the studied L-shaped meta-atom with the following variables, *d* is the width of each arm, *l* is the offset length for the x-oriented arm and *h* is the length of the y-directed arm.

Three different sizes of L-shaped meta-atoms were studied, which we will refer to as small, medium and large. All L-shapes were 75 nm thick. We fixed the *d* values for the small, medium and large L-shaped meta-atoms at 87 nm, 130 nm, and 195 nm, respectively. The area *A* within each size range of L-shaped meta-atom was held constant, and the y-oriented arm length *h* was calculated by the formula

$$h = A/d - l \tag{5}$$

Optics EXPRESS

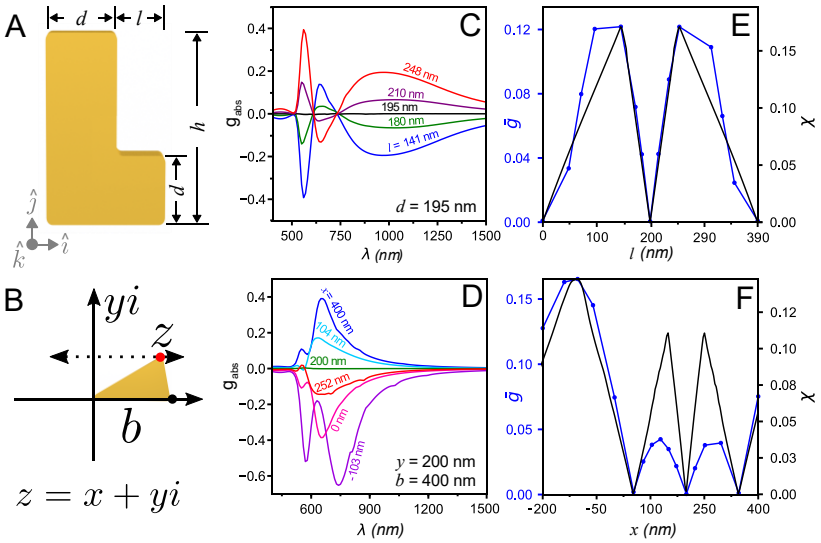

Fig. 2. Calculated circular differential optical absorption and geometric chirality for L-shaped and triangle meta-atoms. (a) Sketch of the parameterized L-shaped meta-atom. The structure sits in the x–y plane and is excited with a plane wave in the –z-direction. (b) Circular differential anisotropy factor, g_{abs} for large Au L-shapes with select l values, d = 195 nm and h values calculated using Eq. (5). (c) The integrated circular differential anisotropy factor, $\bar{g}$ (blue) and the chiral coefficient, χ (black) for large Au L-shaped meta-atoms calculated for all l values. (d) Sketch of triangular meta-atom with a base width, b of 400 nm. Two vertices defining the base of the triangle are fixed (origin and black dot). The third point is defined by $z = x + yi$ with y fixed at 200 nm. (e) Circular differential anisotropy factor, g_{abs} for triangles with select x values. (f) The integrated circular differential anisotropy factor, $\bar{g}$ (blue) and the chiral coefficient, χ (black) for triangular meta-atoms for all calculated x values.

To initially assess the CDOA we calculated g_{abs} for various L-shaped meta-atoms using Eq. (1). In Fig. 2(b) we report the effect of varying l on the calculated wavelength dependent g_{abs} values for large Au L-shaped meta-atoms with a fixed d of 195 nm. It is important to note that when we vary l, h changes as well in order to keep the area, A, of the L-shaped meta-atom constant. For clarity purposes, we only show five different l values in Fig. 2(b). We report the complete g_{abs} spectra for all calculated L-shaped meta atoms, small, medium, and large, in the appendix. The g_{abs} spectra in Fig. 2(b) for the L-shaped meta-atom show a strong trisignate feature covering the visible and near-infrared regions with sharp peaks at 550 and 650 nm and a single broad peak centered at ~900 nm, which we label L_{550}, L_{650}, and L_{900} respectively. The calculated g_{abs} for the L-shaped meta-atom is zero for all wavelengths when l is 0 nm, 195 nm, and 390 nm—an x-oriented rod, an L-shape with equidistant arms, and an y-oriented rod—respectively. This result is expected since for all three of these cases the particle exhibits both M_{xy} and C_2 symmetry resulting in no CDOA. We observed the general trend in the magnitude of the three g_{abs} peaks as l is increased. All three peaks increase in magnitude, reaching a local maximum when $l = 141$ nm and $h = 443$ nm. When l is increased above 141 nm, the magnitude of the g_{abs} peaks decrease, returning to zero magnitude when $l = 195$ nm, the equidistant arm length. For $l > 195$ nm the three g_{abs} peaks change signs and increase in magnitude, reaching a local maximum for the L_{900} peak at $l = 248$ nm and $h = 337$ nm. For $l > 306$ nm the magnitude for all three g_{abs} peaks decreases, returning to zero when $l = 390$ nm, the x-oriented rod geometry.

Optics EXPRESS

Comparing the calculated peak magnitudes from g_{abs} spectra for various L-shaped meta-atoms provides a measure of the effect geometry has on the individual g_{abs} peaks. Unfortunately, peak magnitude alone is not a good judge of broadband CDOA, since a peak could have a large magnitude but a narrow full width at half maximum (FWHM). To more accurately quantify the broadband CDOA from an L-shaped meta-atom, we numerically integrated the absolute value of its g_{abs} spectra over the 400 – 1500 nm wavelength range, which covers the primary optical response of the material. We divided the result of the numerical integration of $|g_{abs}|$ by the length of the integration interval to yield dimensionless $\bar{g}$ (Eq. (3)) at specific geometric conditions for each meta-atom. To the best of our knowledge, $\bar{g}$ is a new metric for quantifying broadband CDOA from plasmonic nanostructures. We used the absolute value of g_{abs} in the integration to avoid left- and right-handed CDOA from cancelling each other out. In Fig. 2(c) we plot $\bar{g}$ (blue) using the g_{abs} spectra calculated from large L-shaped Au meta-atoms. The $\bar{g}$ plot shows two maxima and three points where $\bar{g} = 0$. The two largest $\bar{g}$ values, which we define as the geometric conditions with the largest broadband CDOA response, occur when $l = 168$ and 263 nm. These l values correspond to L-shaped meta-atoms with $h = 416$ nm and $h = 322$ nm, respectively. The three $\bar{g} = 0$ points occur when the meta-atom is an x- or y-oriented rod, i.e. when $l = 0$ or 390 nm, or when the L-shaped meta-atom has equidistant, arms, i.e. when $l = 195$ nm. Starting from $l = 0$, $\bar{g}$ rises as l increase reaching, a local maximum of ~0.125 at $l = 168$ nm. As l increases beyond 168 nm, $\bar{g}$ decreases, returning to zero at $l = 195$ nm, where the arms are equal lengths. For $l > 195$ nm, $\bar{g}$ increases again, reaching a local maximum of ~0.125 when $l = 263$ nm. When l is longer than 263 nm, $\bar{g}$ decreases and returns to zero when $l = 390$ nm, the y-oriented rod geometry.

We compared the electromagnetic response with the geometric chirality of the L-shaped meta-atoms by overlaying the integrated CDOA, $\bar{g}$ (blue), and the chiral coefficient, χ (black), in Fig. 2(c) for l values from 0 to 390 nm. A very strong correlation exists between $\bar{g}$ and χ with a calculated Pearson correlation coefficient [38] (PCC) of 0.95. A PCC of one indicates a perfect positive linear correlation between the two variables. The two plots have maxima at $l = 142$ nm and 263 nm. Furthermore, both $\bar{g}$ and χ are equal to zero when $l = 0$, 195, or 390 nm, i.e. cases where the meta-atom has both C_2 and M_{xy} symmetry. $\bar{g}$ and χ for the small and medium sized Au L-shaped meta-atoms with l values from 0 to 173 nm and 0 to 260 nm, respectively, also show an excellent correlation, as shown in the appendix. Remarkably, despite significant differences in the g_{abs} plots for the small, medium and large L-shaped Au meta-atoms we observe a strong correlation between all of their $\bar{g}$ and χ values with PCCs of 0.95 or higher.

3.2 Triangular meta-atoms

Several research groups have explored the plasmon resonances from equilateral triangular plates, also called nanoprisms, using both far- and near-field spectroscopy [39–41]. These groups report dipole and multipole plasmon resonances in nanoprisms [39] spanning the visible and near-infrared spectrum [41]. In general, as nanoprisms increase in size their dipole resonances broaden and shift to lower energy while multipole modes appear at higher energies [40]. To the best of our knowledge, the optical properties from non-equilateral, e.g., right, obtuse or acute, plasmonic triangular nanostructures have not been reported. The purely geometric chirality of non-equilateral triangles has been extensively studied by others with several reports concluding that any scalene triangle can be the most chiral depending on the

Optics EXPRESS

geometric chiral measure used in the analysis [42,43]. In order to focus on general trends, we employ only a single chiral measure, Gilat's chiral coefficient, χ, and compare it to the integrated CDOA, $\bar{g}$, for a wide range of triangles.

Figure 2(d) details how we parameterized the geometry of the triangular meta-atom. Two points of the triangle are fixed which define the base vertices. We will refer to the length of the base as *b*. The third point of the triangle, *z*, is defined by the equation $z = x + yi$, where *x*, and *y* are the distances along the *x*- and *y*-axes, respectively. We fixed *y* at 200 nm and swept *x* from −200 to 400 nm with sixteen different points. This x-range allowed us to sample scalene, isosceles, and right triangles, as well as triangles with one obtuse angle which exhibit a high degree of geometric chirality. Furthermore, x-values lower than −200 nm create triangles with extremely sharp corners which would be impossible to realize experimentally. The area of the triangles was fixed. All triangles were 100 nm thick. To understand the wavelength dependence of the CDOA we plot g_{abs} in Fig. 2(e) for select *x* values. g_{abs} spectra for all *x* values studied is included in the appendix. Right, obtuse and acute triangles in Fig. 2(e) have two g_{abs} peaks. Isosceles triangles have C_2 rotational symmetry along their bisector and therefore show no CDOA. In Fig. 2(e) we observe this effect for the isosceles triangle at *x* = 200 nm which has a g_{abs} of zero for all wavelengths.

As with the L-shaped meta-atoms, it is difficult to judge the broadband CDOA of the triangles by their g_{abs} spectra. In Fig. 2(f) we plot $\bar{g}$ (blue) for triangular meta-atoms with sixteen different *x* values from −200 to 400 nm. The resulting $\bar{g}$ vs. *x* plot has one global maximum, two local maxima and three points where $\bar{g}$ is equal to zero. The three *x* values at 53, 200 and 346 nm where $\bar{g}$ is equal to zero correspond to three different isosceles triangles. Each of these isosceles triangles has C_2 rotational symmetry and therefore no CDOA. The C_2 symmetry axis is perpendicular to the single unequal side of the triangle and intersect that side at the given *x* value. Three local maxima in $\bar{g}$ are formed when *x* = −103 nm, 128 and 296 nm. The triangle at *x* = −103 nm is obtuse with the global maximum $\bar{g}$ value of 0.16. The two meta-atoms formed at *x* = 128 and 296 nm are both acute triangles with $\bar{g}$ values of 0.042 and 0.040, respectively.

To test the correlation between $\bar{g}$ and χ for the triangular meta-atoms we overlaid the χ vs. *x* values (black) on Fig. 2(f). Like we observed for the L-shaped meta-atoms, we see a good correlation between the integrated CDOA values, $\bar{g}$ and the geometric chirality, χ for the triangular meta-atoms with a PCC of 0.78. The *x* values for the global maximum, the two local maxima and all three zero values for both $\bar{g}$ and χ show good agreement. The scaling of $\bar{g}$ shifts with respect to χ when the geometry passes through one of the zero χ points at *x* = 53 nm. To the left of this point, the triangle geometry has an obtuse angle and is more elongated compared to the acute triangles generated when x is above 53 nm. We believe the change in the triangle geometry from obtuse to acute is responsible for the change in $\bar{g}$ scaling.

3.2 Dimer meta-atoms

Local surface plasmon modes from individual meta-atoms can couple, or "hybridize" when their near fields are brought within proximity to each other [44]. The optical activity of coupled plasmonic nanoparticle assemblies have been widely reported by several groups [45,46]. Dimers represent the simplest geometry which can exhibit plasmon coupling [47]. Halas *et al.* reported that nanorod dimer interactions are both orientation and polarization dependent [48]. Planar nanorod dimers, while not supporting true optical activity, can exhibit two-dimensional chirality [17]. We investigated whether the correlation between geometric chirality and broadband CDOA would also exist for nanorod dimers which can exhibit plasmonic coupling

Optics EXPRESS

effects. Our dimer structure consists of two nanorods of width, *a*, length, *b*, a y-offset of, *d*, and an x-offset of, *r*, shown in Fig. 3(a).

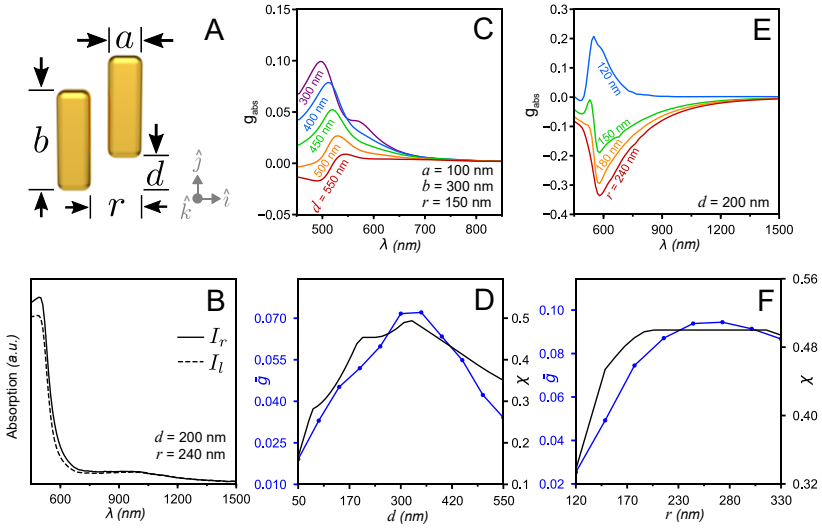

Fig. 3. Calculated circular differential optical absorption and geometric chirality for the dimer meta-atoms. (a) Sketch of parameterized dimer meta-atom with *b* as the dimer height, *a* the width, *d* the vertical offset distance, and *r* the horizontal offset distance. (b) Absorption plots, I_r and I_l, for the dimer at *r* = 240 nm, *d* = 200 nm excited with RCPL and LCPL orthogonal to the plane of the paper, respectively. (c) Circular differential anisotropy factor, g_{abs} for dimers with select *d* values. (d) The integrated circular differential anistropy factor, $\bar{g}$ (blue) and the chiral coefficient, χ (black) for dimers for all calculated *d* values. (e) Circular differential anisotropy factor, g_{abs} for dimers with select *r* values. (f) The integrated circular differential anistropy factor, $\bar{g}$ (blue) and the chiral coefficient, χ (black) for dimers for all calculated *r* values.

The individual nanorods exhibit no geometric chirality. However, χ is nonzero when the two nanorods are treated as one structure and analyzed in two-dimensional space. Moreover, their CDOA is nonzero due to the strong polarization dependence of their plasmon modes [48]. Fig. 3(b) shows the absorption spectra for a dimer excited with LCPL and RCPL. The dimer in Fig. 3(b) has an *r* = 240 nm, *d* = 200nm, *a* = 100 nm, and *b* = 300 nm. All dimers were 100 nm thick. Polarization dependent absorption is clear for all wavelengths under 1200 nm. Since both the geometric chirality and the degree of plasmonic coupling depend on the spacing between the nanorods, we simulated the shapes and computed g_{abs} for dimers with varying *d* and varying *r* values. In both cases, the width of each nanorod, *a*, was constant at 100 nm, as well as the height, *b*, at 300 nm. In the first set of simulations, the *d* parameter was varied between 50 nm and 550 nm, keeping *r* at 150 nm. Select computed g_{abs} spectra are shown in Fig. 3(c). At *d* = 300 nm we observe a g_{abs} peak at ~500 nm with a shoulder at ~580 nm. As the *y*-offset between the nanorods, *d*, is increased, the shoulder at ~580 nm is suppressed, and the 500 nm peak is both red-shifted and suppressed. The full set of g_{abs} spectra for *d*-values between 50 nm and 550 nm is presented in the appendix.

To assess the effect of varying the *y*-offset, *d*, on the broadband CDOA of the dimer meta-atoms we used Eq. (3) to calculate $\bar{g}$ for each of the g_{abs} spectra. Figure 3(d) shows the resulting broadband CDOA, $\bar{g}$, (blue) plotted vs. *y*-offset, *d*, for the dimer meta-atoms. A maximum $\bar{g}$ is obtained at *d* = ~300 nm with shorter and longer *y*-offset values resulting in lower $\bar{g}$ values. When the y-offset between the nanorods is greater than 300 nm, the $\bar{g}$ for the

Optics EXPRESS

dimer assembly decreases rapidly. This rapid reduction in broadband CDOA can be understood based on the interaction energy between the nanorods, which we approximate as dipoles [48]. The interaction energy for dipoles is proportional to $1/r^3$ with *r* being the interparticle distance [48]. Therefore, as the nanorods move apart, their coupling strength decreases and the meta-atom appears more like two individual nanorods to the incoming plane wave. To assess the correlation between geometric chirality and broadband CDOA we overlaid χ (black) vs. the *y*-offset, *d* in Fig. 3(d). Remarkably, both the maxima for χ and $\bar{g}$ align to excellent agreement when *d* is ~300 nm and an overall PCC of 0.91. As *d* is further increased, the plasmonic coupling of the shapes weakens and $\bar{g}$ drops more rapidly than χ. This effect is to be expected given the before mentioned interaction energy. Once again, the physical parameters of the system are of critical importance. However, the correlation between χ and $\bar{g}$ for the dimer meta-atom illustrates the versatility of this tool for optimizing structures for maximum broadband CDOA; even non-contiguous meta-atoms are applicable.

Next, we simulated dimer meta-atoms with varying *x*-offset, *r*, between 120 and 330 nm with *d* fixed at 200 nm. g_{abs} spectra were computed and select spectra are shown in Fig. 3(e). g_{abs} spectra for all *r*-values are plotted in the appendix. At *r* = 120 nm there is a single positive peak in the g_{abs} spectra at ~560 nm which falls rapidly at longer wavelengths. When the *x*-offset, *r*, is increased to 150 nm the positive peak at ~560 nm is suppressed and a new negative peak at ~580 nm appears. Further increases in *r* to 240 nm result in the ~560 nm peak becoming a shoulder to the primary peak at ~580 nm. The value of both peaks becomes more negative as *r* is increased to 240 nm. Beyond *r* = 240 nm the primary peak at ~580 nm starts to decrease, presumably because the interaction energy between the two nanorods is decreasing. Figure 3(f) shows the integrated broadband CDOA, $\bar{g}$, (blue) plotted vs. *x*-offset, *r*, for the dimer meta-atoms. The broadband CDOA, $\bar{g}$, increases with increasing *r*-values to a maximum of ~0.09 at *r* = 240 nm. Larger *x*-offset values decrease $\bar{g}$, again presumably due to the reduction in interaction energy between the nanorods as they are spaced farther apart. In Fig. 3(f) we also plot the chiral coefficient, χ, (blue) to assess the correlation between broadband CDOA and geometric chirality. Again we see a strong correlation between the two plots with a PCC of 0.93, demonstrating the flexibility of the chiral coefficient for optimizing both contiguous and non-contiguous plasmonic structures. In principle, as long as the shapes are electromagnetically coupled, any number of meta-atoms could be placed together and their χ value optimized to engineer large CDOA.

Optics EXPRESS

3.4 Origin of CDOA

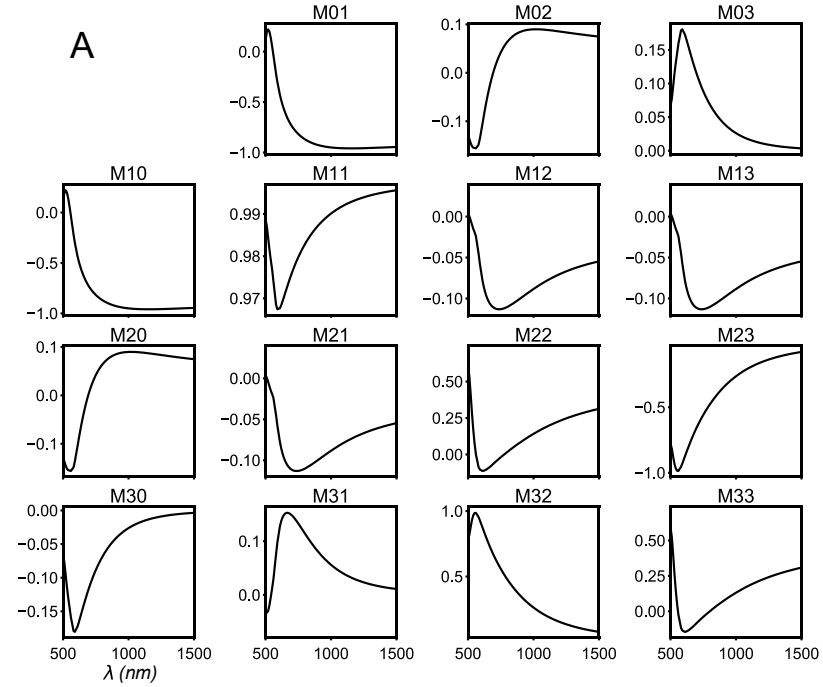

B

$$\mathbf{M} = exp(\mathbf{L}) = exp\begin{pmatrix} A & -LD & -LD' & CD \\ -LD & A & CB & LB' \\ -LD' & -CB & A & -LB \\ CD & -LB' & LB & A \end{pmatrix}$$

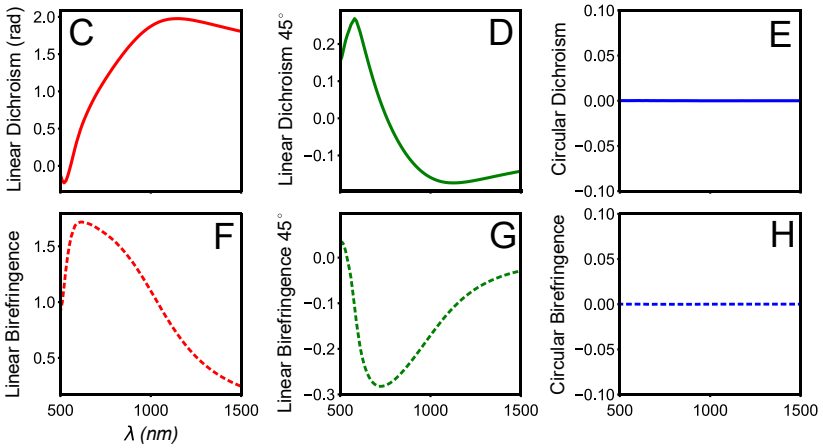

Fig. 4. (a) Calculated Mueller matrix for the Au dimer meta-atom which demonstrated both maximum broadband differential absorption, $\overline{g}$, and geometric chirality, χ. The geometric parameters for the meta-atom are, a = 100 nm, b = 300 nm, r = 240 nm and, d = 200 nm. (b) Eq. (4) relating the Mueller Matrix to the six fundamental optical polarization effects. (c - h) The six elementary optical polarization properties for a dimer meta-atom in (a) calculated using the analytical inversion method [4]. This meta-atom does not show optical activity but rather a combination of linear optical polarization effects.

Optics EXPRESS

To better understand the polarization properties of the meta-atoms and the origin of their CDOA we calculated the Mueller matrices for each meta-atom at the geometric conditions corresponding to their maximum $\bar{g}$ and χ values. The Mueller matrix contains complete information about the polarization effects for an optical element at a given excitation wavelength and angle of incidence [28,30]. Figure 4(a) shows the Mueller matrix for a dimer with an r of 240 nm and a d of 200 nm. This geometry corresponds to the largest χ and $\bar{g}$ values in the simulations where r was varied with a maximum $\bar{g}$ of 0.094 and a maximum χ of 0.50. To understand the polarization effects leading to CDOA in the dimer, we investigate the relationships between the individual elements in the Mueller matrix. The concept of Minkowski-symmetry is useful to differentiate between CDOA and true optical activity. Minkowski space is a four dimensional space in (x,y,z,t). Minkowski symmetry in optics means that the effects of an optical element are equivalent under a transformation reversing time or, equivalently, the sample orientation. Arteaga *et al*. reported that a Mueller matrix which does not satisfy all of the following relationships, $\mathbf{M_{01}} = \mathbf{M_{10}}$, $\mathbf{M_{02}} = -\mathbf{M_{20}}$, $\mathbf{M_{03}} = \mathbf{M_{30}}$, $\mathbf{M_{12}} = -\mathbf{M_{21}}$, $\mathbf{M_{13}} = \mathbf{M_{31}}$ and $\mathbf{M_{23}} = -\mathbf{M_{32}}$ is non-Minkowski symmetric [10]. The Mueller matrix for the dimer fails four out of the six criteria. Specifically, the conditions $\mathbf{M_{02}} = -\mathbf{M_{20}}$, $\mathbf{M_{03}} = \mathbf{M_{30}}$, $\mathbf{M_{12}} = -\mathbf{M_{21}}$ and $\mathbf{M_{13}} = \mathbf{M_{31}}$ are not met. Arteaga *et al*. attributed the non-Minkowski symmetric Mueller matrix from oblique two-dimensional hole arrays to misaligned surface plasmon modes [9]. When Arteaga *et al.* turned the hole arrays over their sense of misalignment changed resulting in asymmetric transmission of CPL, which is not to be confused with optical activity which manifests as CD and CB [9]. Asymmetric transmission of CPL was first observed by Fedotov et al. for planar chiral media like we study in the present work [19]. Clearly, the Mueller Matrix for the dimer meta-atom is also non-Minkowski symmetric which we hypothesize is due to misaligned surface plasmon modes. The Mueller matrix of homogeneous, non-depolarizing media can be described by seven fundamental parameters using the differential Mueller matrix, **L**, see Fig. 4(b). Assuming zero depolarization, which we verified by calculating a depolarization index [32,33,49] of one for all the meta-atoms, we used the analytical inversion method [4] to calculate the differential Mueller matrix, **L** and determine the polarization effects from each meta-atom and ultimately better understand the origin of their CDOA. It is important to note that calculating the exponent of a matrix is non-trivial and therefore symmetries which appear in a Mueller matrix may not appear in **L**. Figures 4(c)-4(h) shows the calculated six fundamental optical polarization effects of the Au dimer in Fig. 4(a). We find that both CD and CB are zero as expected, and that linear optical polarization effects from LD, LD', LB and LB' are responsible for CDOA [50], not true optical activity. The equation for CDOA as measured by a circular dichroism spectrometer is:

$$CDOA = G_0\{CD + \frac{1}{2}(LD'LB - LDLB') + (LD'\sin(2\theta) - LD\cos(2\theta)\sin(\alpha)\} \quad (6)$$

Where G_0 is the apparatus constant, CD is circular dichroism from true optical activity, θ is the sample rotation and α represents the non-ideal strain in the photoelastic modulator [50]. In our simulations, θ and α are both zero. CD is also zero since two-dimensional meta-atoms are not optically active, resulting in the simplified version of Eq. (6), $CDOA = (G_0/2)(LD'LB - LDLB')$. Moreover, the magnitude of $(LD'LB - LDLB')$ correlates with the magnitude of g_{abs} for all the simulated spectra. CDOA in the L-shaped and triangular meta-atoms is also driven by a combination of linear optical polarization effects vs. optical activity. The six elementary polarization properties for the L-shaped and triangle meta-atoms are included in the appendix.

Optics EXPRESS

4. Summary

In summary, we have demonstrated that the geometric chirality of various two-dimensionally chiral meta-atoms displays a strong correlation to their calculated broadband circular differential optical absorption (CDOA). We performed full-field electromagnetic simulations of Au L-shapes, triangles and nanorod dimer meta-atoms over a broad wavelength range (400 – 1500 nm). We calculated the anisotropic dissymmetry factor, g_{abs} as a function of wavelength for the three meta-atoms over a wide set of geometric conditions. To better quantify the broadband CDOA from these meta-atoms, we integrated g_{abs} over the full wavelength range to produce a new metric, the integrated anisotropic dissymmetry factor, $\bar{g}$. We rapidly calculate the geometric chirality for all three meta-atoms over the same set of geometric conditions using a known overlap method. We show a strong correlation between the broadband CDOA and the geometric chirality for all three meta-atoms. Furthermore, the geometric parameters for objects with maximum geometric chirality correspond exceptionally well to objects with maximum broadband CDOA. Lastly, we calculate the Mueller matrices and the associated six fundamental polarization effects for each meta-atom geometry and determine that linear optical polarization effects, not true optical activity, are the cause of the CDOA in all three structures. A potential application for this correlation is the rapid optimization of plasmonic nanostructures for maximum broadband CDOA.

Appendix

1. L-shaped meta-atoms results

In addition to the work already shown, different scales of L-shaped meta-atoms were studied.

Complete g_{abs} spectra for the L-shaped meta atoms studied with varying l parameter are shown below in Fig. 5. The correlation between χ and $\bar{g}$ is shown in Fig. 6 for the large and medium sized L-shapes. For all the size scaled studied, the correlation between χ and $\bar{g}$ is excellent.

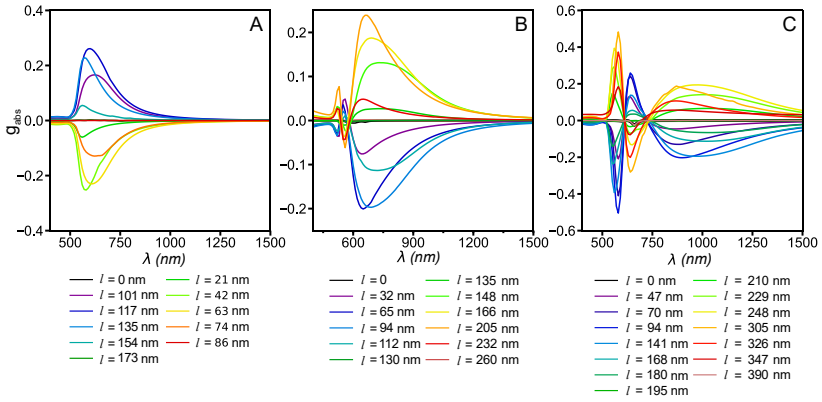

Fig. 5. Calculated g_{abs} spectra for (a) small (A = 22500 nm^2, d = 87 nm), (b) medium, (A = 50700 nm^2, d = 130 nm), and (c) large (A = 114100 nm^2, d = 195 nm), Au L-shaped meta-atoms for all studied l values.

Optics EXPRESS

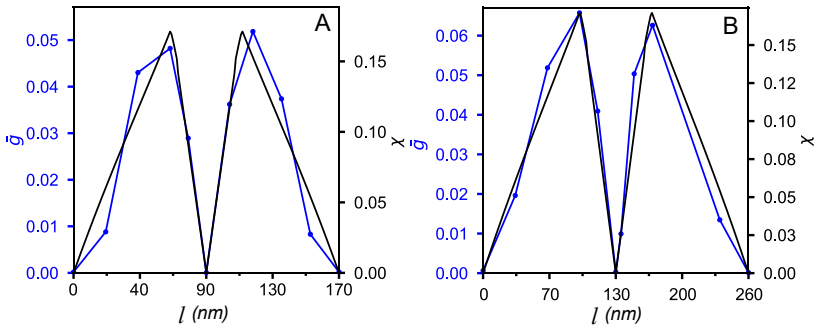

Fig. 6. Integrated circular differential anisotropy factor, $\bar{g}$ blue, and chiral coefficient χ (black) vs. *l* for (a) small and, (b) medium sized Au L-shaped meta-atoms.

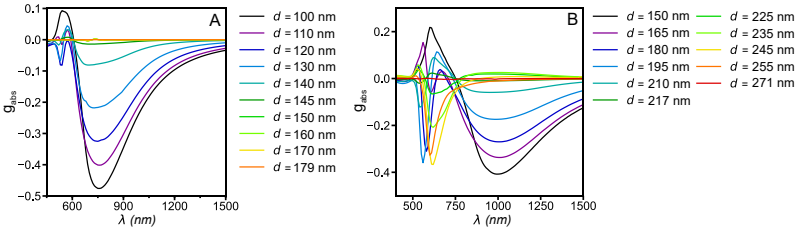

Fig. 7. g_{abs} spectra for (a) medium and (b) large L-shaped Au meta-atoms with varying *d* values and *l* fixed at (a) 100 nm and (b) 150 nm.

We also explored the effect of varying the arm width, *d*, on the calculated wavelength dependent g_{abs} values for medium and large Au L-shaped meta-atoms. Wavelength dependent g_{abs} spectra from 400 – 1500 nm for various d values are shown below in Fig. 7**.** In Fig. 8 we plot the $\bar{g}$ (blue) values vs. *d* for the g_{abs} spectra in Fig. 8 using Eq. (3). Initially, we studied the effect of varying the arm width, *d*, on $\bar{g}$ for medium sized Au L-shaped meta-atoms. Figure 8(a) plots $\bar{g}$ and χ with good agreement for $d < 145$ nm. When $d > 145$ nm, the correlation between $\bar{g}$ and χ breaks down. We believe this is because the dimensions of the notch in the medium L-shaped meta-atom become far smaller than the incident light. The dimensions of the notch are characterized by l and $h-d$. For example, at $d = 150$ nm and $l = 100$ nm, $h - d$ is ~90 nm. Notably, for the large L-shaped meta-atom in Fig. 9(b), we did not observe a breakdown in the correlation between $\bar{g}$ and χ at large *d* values. We believe this is because for the large meta-atom, all lengths are 1.5 times larger than the medium-scale L, therefore $h-d$ and l are closer to the wavelength of light. χ, on the other hand, is scale invariant. Clearly, there are limitations to assessing the optical properties of plasmonic nanostructures by pure geometric means. While the correlation between $\bar{g}$ and χ is not as strong as we reported for the *l* sweep in Fig. 2(c), χ for the *d* sweep follows a similar trend as $\bar{g}$. χ predicts the zero points in $\bar{g}$ when the L-shaped meta-atom has equidistant arms or when the meta-atom becomes an *x*-oriented rod. In Fig. 8(b), the primary difference between the correlations on either side of the zero $\bar{g}$ and χ point at $d = 218$ nm is the scaling differences between the local maxima in $\bar{g}$ and their associated χ values. Because the L-shape geometries to the left of the zero χ point at $d = 218$ nm have more elongated legs than those on the right side, the edge-to-edge lengths of the shapes differ significantly, thus the energies of plasmonic resonant modes are also expected to differ. Consequently, absorption behavior is impacted at all wavelengths. Notably, the g_{abs} spectra in Fig. 7(b) lose the broad g_{abs} peak centered at 1000 nm as *d* is increased to 218 nm

Optics EXPRESS

and beyond. We also note that χ begins to decrease as d falls below ~110 nm and ~170 nm in Figs. 8(a) and 8(b)**,** respectively, while $\bar{g}$ continues to increase.

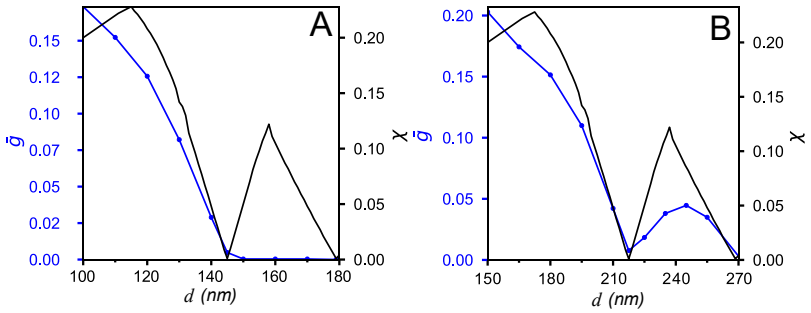

Fig. 8. Integrated circular differential anisotropy factor, $\bar{g}$ (blue), and chiral coefficient χ (black) vs. d for (a) medium and (b) large L-shaped Au meta-atoms with l fixed at a) 100 nm and b) 150 nm.

We suspect the discrepancy between $\bar{g}$ and χ when d is small is due to the increase in the total edge length of the L-shape meta-atom which results in significant edge-effects that are not predicted by our measure of geometric chirality. To better understand the polarization properties of the L-shaped meta-atom and the origin of CDOA, we calculated the optical effects for a large Au L-shaped meta-atom at its maximum $\bar{g}$ and χ values. Figure 9 shows the optical effects for this L-shape with l = 248, h = 337 and d = 195 nm. This L-shaped meta-atom gave significant CDOA, with a maximum $\bar{g}$ of 0.120 and a maximum χ of 0.171. The Mueller Matrix for the large L-shaped meta-atom is non-Minkowski symmetric which we hypothesize is due to misaligned surface plasmon modes. We find that both CD and CB are zero as expected, and that linear optical effects from LD, LD', LB, and LB' are responsible for CDOA [50], not true optical activity. We also calculated the polarization properties for a medium L-shaped meta-atom with d = 160 nm, shown in Fig. 10. This geometry is within the region where the correlation between $\bar{g}$ and χ break down in Fig. 8(a). We found that the Mueller matrix are Minkowski symmetric and the polarization properties show both zero LD' and LB' cross the entire wavelength region.

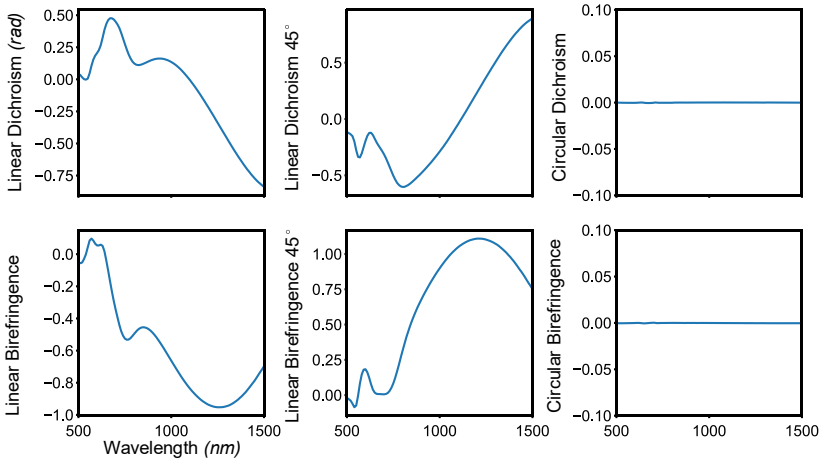

Fig. 9. The six elementary polarization properties for a large L-shaped meta-atom with l = 248 nm, h = 337 nm and d = 195 nm. The meta-atom does not show optical activity but rather linear optical effects.

Optics EXPRESS

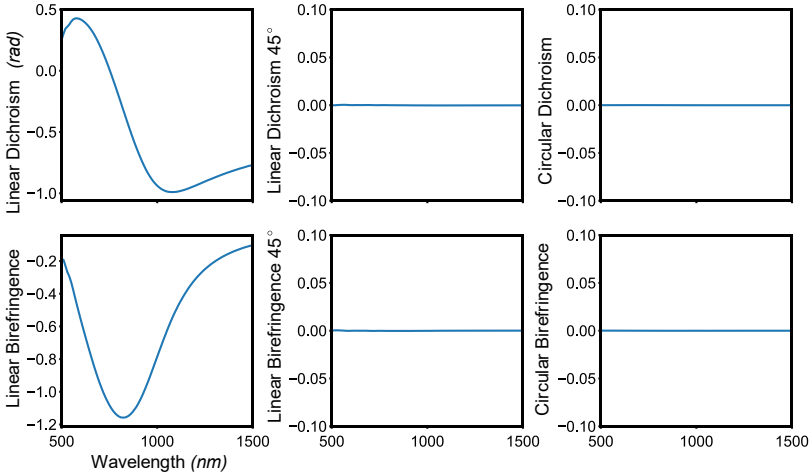

Fig. 10. The six elementary polarization properties for the medium-scale Au L-shaped meta-atoms with l = 100 nm, h = 217 nm and d = 160 nm. The lack of LD45 and LB45 is consistent with zero CDOA shown in Fig. 8(a) for d-values > 145 nm.

2. Triangular meta-atoms results

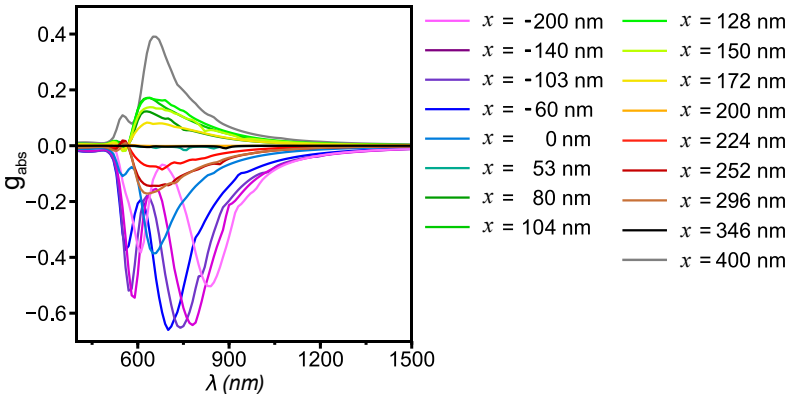

Fig. 11. g_{abs} spectra for the triangle meta-atoms for all x values with a base length b = 400 nm and y = 200 nm for the upper vertex position defined by $z = x + yi$

g_{abs} spectra from 400 – 1500 nm for triangles of various x values are shown in Fig. 11. To better understand the polarization properties of the triangular meta-atoms, we calculated the Mueller matrix for the triangle with maximum $\bar{g}$ and χ values found at x = –103 nm. Like we found for the L-shaped meta-atom, the Mueller matrix for the triangular meta-atom is non-Minkowski symmetric with the following four out of the six criteria not being satisfied, $\mathbf{M_{02}} = \mathbf{-M_{20}}$, $\mathbf{M_{03}} = \mathbf{M_{30}}$, $\mathbf{M_{12}} = \mathbf{-M_{21}}$, and $\mathbf{M_{13}} = \mathbf{M_{31}}$. Fig. 12 shows the calculated polarization optical effects of the selected triangular meta-atom. Again, similar to the L-shape meta-atom, we find that both CD and CB are zero as expected, and that linear polarization effects from LD, LD', LB, and LB' are responsible for CDOA, not true optical activity.

Optics EXPRESS

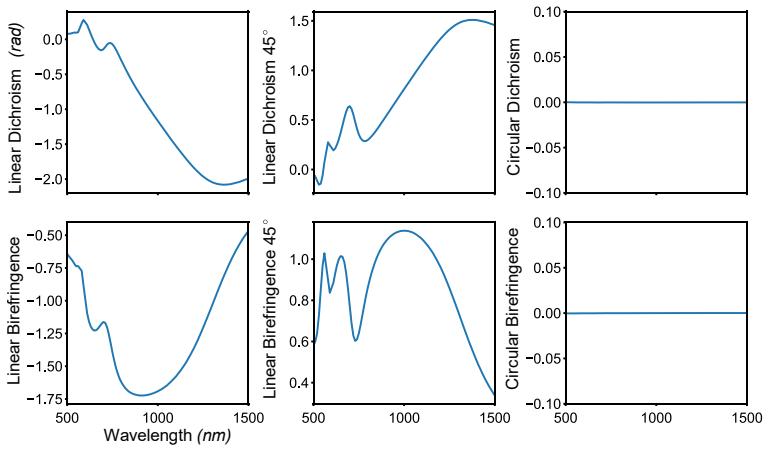

Fig. 12. The six elementary polarization properties for an obtuse triangle meta-atom with x = –103 nm and y = 200 nm which demonstrated both maximum broadband differential absorption, $\overline{g}$ and geometric chirality, χ. The meta-atom does not show optical activity but rather linear polarization effects.

3. Dimer meta-atoms

g_{abs} spectra from 450 – 850 nm are shown for various dimer meta-atoms with varying d spacing in Fig. 13, and spectra from 500 – 1500 nm are shown with varying r spacing in Fig. 14.

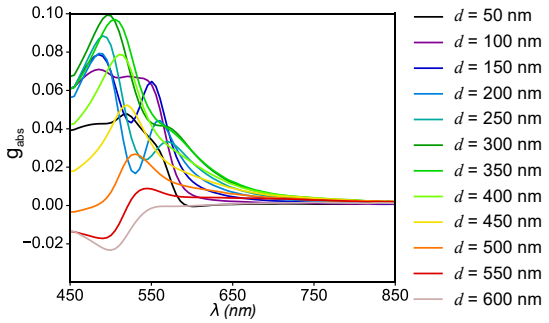

Fig. 13. g_{abs} spectra for the dimer Au meta-atoms with d varied, r fixed at 150 nm, a fixed at 100 nm, and b fixed at 300 nm.

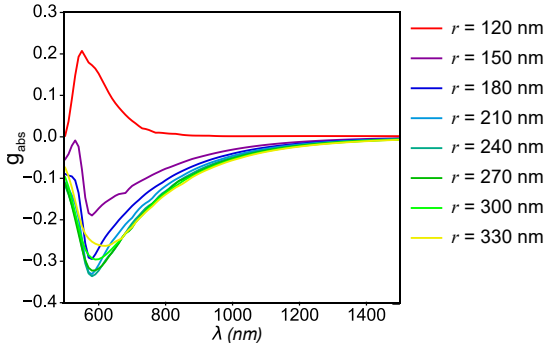

Fig. 14. g_{abs} spectra for the dimer Au meta-atoms with r varied, d fixed at 200 nm, a fixed at 100 nm, and b fixed at 300 nm.

Optics EXPRESS

4. Electromagnetic simulations

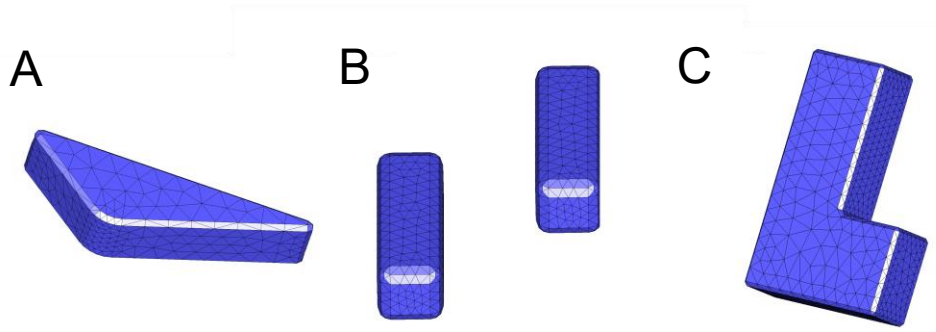

Fig. 15. Examples of meshes used for electromagnetic simulation in JCMwave. (a) Triangular meta-atom with $x = -103$ nm, $y = 200$ nm, $b = 400$ nm. (b) Dimer meta-atom with $d = 200$ nm, $r = 240$ nm, $a = 100$ nm, $b = 300$ nm. (c) L-shaped meta-atom with $l = 100$ nm, $h = 323$ nm, $d = 120$ nm.

We used JCMsuite v3.8.0 software by JCMwave Gmbh for all electromagnetic simulations. We used a polynomial degree of four for all electromagnetic simulations. An airspace mesh was maintained around all meta-atoms of at least 150 nm. A perfectly matched layer was used with a thickness adapted to each simulation; PML thickness was tuned by JCMsuite's internal algorithm. Typical meshes for each geometry of meta-atom are shown in Fig. 15. For the calculation of the Mueller Matrices, JCMsuite's postprocessing code was used on the meta-atom simulation data with a pair of X and Y linearly polarized plane wave sources. A Fourier transform was performed on the file containing the electric field tensor in order to calculate the reflected modes. We used a numerical aperture of 0.1 and a normal direction of Z for the Fourier transform. The Mueller Matrices were calculated from the reflected modes. More information about the procedure for computing these quantities is available in the JCMsuite online documentation.

5. Chiral coefficient code

Python code used to compute the chiral coefficient for 2D shapes is available online at: https://gitlab.com/mcpeaklab/chiral-coefficient.

Funding

National Science Foundation (NSF) Early CAREER Award (1653705); Freie Universität Berlin through the Dahlem Research School; EU (H2020) (EMPIR-17FUN01).

Acknowledgments

This project has received funding from the EMPIR programme co-financed by the Participating States and from the European Union's Horizon 2020 research and innovation programme under grant agreement number 17FUN01 (BeCOMe).

Disclosures

The authors declare that there are no conflicts of interest related to this article.

References

1. W. Li, Z. J. Coppens, L. V. Besteiro, W. Wang, A. O. Govorov, and J. Valentine, "Circularly polarized light detection with hot electrons in chiral plasmonic metamaterials," Nat. Commun. **6**(1), 8379 (2015).
2. E. Hendry, T. Carpy, J. Johnston, M. Popland, R. V. Mikhaylovskiy, A. J. Lapthorn, S. M. Kelly, L. D. Barron, N. Gadegaard, and M. Kadodwala, "Ultrasensitive detection and characterization of biomolecules using superchiral fields," Nat. Nanotechnol. **5**(11), 783–787 (2010).
3. M. Hentschel, M. Schäferling, T. Weiss, N. Liu, and H. Giessen, "Three-dimensional chiral plasmonic oligomers," Nano Lett. **12**(5), 2542–2547 (2012).

Optics EXPRESS

4. O. Arteaga and A. Canillas, "Analytic inversion of the Mueller-Jones polarization matrices for homogeneous media," Opt. Lett. **35**(4), 559–561 (2010).
5. H. Okamoto, T. Narushima, Y. Nishiyama, and K. Imura, "Local optical responses of plasmon resonances visualised by near-field optical imaging," Phys. Chem. Chem. Phys. **17**(9), 6192–6206 (2015).
6. J. T. Collins, C. Kuppe, D. C. Hooper, C. Sibilia, M. Centini, and V. K. Valev, "Chirality and chiroptical effects in metal nanostructures: Fundamentals and current trends," Adv. Opt. Mater. **5**(16), 1700182 (2017).
7. K. M. McPeak, C. D. van Engers, S. Bianchi, A. Rossinelli, L. V. Poulikakos, L. Bernard, S. Herrmann, D. K. Kim, S. Burger, M. Blome, S. V. Jayanti, and D. J. Norris, "Ultraviolet plasmonic chirality from colloidal aluminum nanoparticles exhibiting charge-selective protein detection," Adv. Mater. **27**(40), 6244–6250 (2015).
8. K. M. McPeak, C. D. van Engers, M. Blome, J. H. Park, S. Burger, M. A. Gosálvez, A. Faridi, Y. R. Ries, A. Sahu, and D. J. Norris, "Complex chiral colloids and surfaces via high-index off-cut silicon," Nano Lett. **14**(5), 2934–2940 (2014).
9. O. Arteaga, J. Sancho-Parramon, S. Nichols, B. M. Maoz, A. Canillas, S. Bosch, G. Markovich, and B. Kahr, "Relation between 2d/3d chirality and the appearance of chiroptical effects in real nanostructures," Opt. Express **24**(3), 2242–2252 (2016).
10. O. Arteaga, B. M. Maoz, S. Nichols, G. Markovich, and B. Kahr, "Complete polarimetry on the asymmetric transmission through subwavelength hole arrays," Opt. Express **22**(11), 13719–13732 (2014).
11. O. Arteaga, "Number of independent parameters in the Mueller matrix representation of homogeneous depolarizing media," Opt. Lett. **38**(7), 1131–1133 (2013).
12. A. Schönhofer and H.-G. Kuball, "Symmetry properties of the mueller matrix," Chem. Phys. **115**(2), 159–167 (1987).
13. I. Fernandez-Corbaton, M. Fruhnert, and C. Rockstuhl, "Objects of maximum electromagnetic chirality," Phys. Rev. X **6**(3), 031013 (2016).
14. M. Schäferling, D. Dregely, M. Hentschel, and H. Giessen, "Tailoring enhanced optical chirality: Design principles for chiral plasmonic nanostructures," Phys. Rev. X **2**(3), 031010 (2012).
15. P. Gutsche and M. Nieto-Vesperinas, "Optical chirality of time-harmonic wavefields for classification of scatterers," Sci. Rep. **8**(1), 9416 (2018).
16. P. Gutsche, X. Garcia-Santiago, P.-I. Schneider, K. McPeak, M. Nieto-Vesperinas, and S. Burger, "Role of geometric shape in chiral optics," https://arxiv.org/abs/1808.01855 (2018).
17. L. V. Poulikakos, P. Gutsche, K. M. McPeak, S. Burger, J. Niegemann, C. Hafner, and D. J. Norris, "Optical chirality flux as a useful far-field probe of chiral near fields," ACS Photonics **3**(9), 1619–1625 (2016).
18. D. F. Tang, C. Wang, W. K. Pan, M. H. Li, and J. F. Dong, "Broad dual-band asymmetric transmission of circular polarized waves in near-infrared communication band," Opt. Express **25**(10), 11329–11339 (2017).
19. V. A. Fedotov, P. L. Mladyonov, S. L. Prosvirnin, A. V. Rogacheva, Y. Chen, and N. I. Zheludev, "Asymmetric propagation of electromagnetic waves through a planar chiral structure," Phys. Rev. Lett. **97**(16), 167401 (2006).
20. V. K. Valev, J. J. Baumberg, C. Sibilia, and T. Verbiest, "Chirality and chiroptical effects in plasmonic nanostructures: fundamentals, recent progress, and outlook," Adv. Mater. **25**(18), 2517–2534 (2013).
21. M. Wakabayashi, S. Yokojima, T. Fukaminato, K. Shiino, M. Irie, and S. Nakamura, "Anisotropic dissymmetry factor, g: theoretical investigation on single molecule chiroptical spectroscopy," J. Phys. Chem. A **118**(27), 5046–5057 (2014).
22. P. A. Guye, *Influence de la constitution chimique des dérivés du carbone sur le sens et les variations de leur pouvoir rotatoire* (1890).
23. A. B. Buda, T. A. der Heyde, and K. Mislow, "On quantifying chirality," Angew. Chem. Int. Ed. Engl. **31**(8), 989–1007 (1992).
24. A. Potts, D. M. Bagnall, and N. I. Zheludev, "A new model of geometric chirality for two-dimensional continuous media and planar meta-materials," J. Opt. A **6**(2), 193–203 (2004).
25. A. B. Buda and K. Mislow, "A hausdorff chirality measure," J. Am. Chem. Soc. **114**(15), 6006–6012 (1992).
26. G. Gilat, "Chiral coefficient-a measure of the amount of structural chirality," J. Phys. Math. Gen. **22**(13), L545–L550 (1989).
27. S. Burger, P. Gutsche, M. Hammerschmidt, S. Herrmann, J. Pomplun, F. Schmidt, B. Wohlfeil, and L. Zschiedrich, "Hp-finite-elements for simulating electromagnetic fields in optical devices with rough textures," Proc. SPIE **9630**, 7 (2015).
28. P. Soleillet, "Sur les paramètres caractérisant la polarisation partielle de la lumière dans les phénomènes de fluorescence," Ann. Phys. (Paris) **10**(12), 23–97 (1929).
29. F. Perrin, "Polarization of light scattered by isotropic opalescent media," J. Chem. Phys. **10**(7), 415–427 (1942).
30. H. Mueller, "Memorandum on the polarization optics of the photoelastic shutter," Report of the OSRD project OEMsr-576 **2**(1943).
31. C. F. Bohren and D. R. Huffman, *Absorption and scattering of light by small particles* (John Wiley & Sons, 2008).
32. J. J. Gil and E. Bernabeu, "A depolarization criterion in mueller matrices," Opt. Acta (Lond.) **32**(3), 259–261 (1985).
33. J. J. Gil and E. Bernabeu, "Depolarization and polarization indices of an optical system," Opt. Acta (Lond.) **33**(2), 185–189 (1986).

Optics EXPRESS

34. S. Chandel, J. Soni, S. K. Ray, A. Das, A. Ghosh, S. Raj, and N. Ghosh, "Complete polarization characterization of single plasmonic nanoparticle enabled by a novel Dark-field Mueller matrix spectroscopy system," Sci. Rep. **6**(1), 26466 (2016).
35. J. C. Wilson, P. Gutsche, S. Hermann, S. Burger, and K. M. McPeak, "Chiral coefficient code" (2018), retrieved *https://gitlab.com/mcpeaklab/chiral-coefficient*.
36. C. Menzel, C. Rockstuhl, and F. Lederer, "Advanced jones calculus for the classification of periodic metamaterials," Phys. Rev. A **82**(5), 053811 (2010).
37. J. Yang, J.-S. Zhang, X.-F. Wu, and Q.-H. Gong, "Resonant modes of l-shaped gold nanoparticles," Chin. Phys. Lett. **26**(6), 067802 (2009).
38. K. Pearson, "Note on regression and inheritance in the case of two parents," Proc. R. Soc. Lond. **58**(347-352), 240–242 (1895).
39. L. J. Sherry, R. Jin, C. A. Mirkin, G. C. Schatz, and R. P. Van Duyne, "Localized surface plasmon resonance spectroscopy of single silver triangular nanoprisms," Nano Lett. **6**(9), 2060–2065 (2006).
40. M. Rang, A. C. Jones, F. Zhou, Z.-Y. Li, B. J. Wiley, Y. Xia, and M. B. Raschke, "Optical near-field mapping of plasmonic nanoprisms," Nano Lett. **8**(10), 3357–3363 (2008).
41. K. Imaeda, S. Hasegawa, and K. Imura, "Imaging of plasmonic eigen modes in gold triangular mesoplates by near-field optical microscopy," J. Phys. Chem. C **122**(13), 7399–7409 (2018).
42. A. Rassat and P. W. Fowler, "Any scalene triangle is the most chiral triangle," Helv. Chim. Acta **86**(5), 1728–1740 (2003).
43. A. B. Buda, T. P. E. Auf der Heyde, and K. Mislow, "Geometric chirality products," J. Math. Chem. **6**(1), 243–253 (1991).
44. E. Prodan, C. Radloff, N. J. Halas, and P. Nordlander, "A hybridization model for the plasmon response of complex nanostructures," Science **302**(5644), 419–422 (2003).
45. Z. Fan and A. O. Govorov, "Plasmonic circular dichroism of chiral metal nanoparticle assemblies," Nano Lett. **10**(7), 2580–2587 (2010).
46. V. E. Ferry, M. Hentschel, and A. P. Alivisatos, "Circular dichroism in off-resonantly coupled plasmonic nanosystems," Nano Lett. **15**(12), 8336–8341 (2015).
47. P. Nordlander, C. Oubre, E. Prodan, K. Li, and M. I. Stockman, "Plasmon hybridization in nanoparticle dimers," Nano Lett. **4**(5), 899–903 (2004).
48. N. J. Halas, S. Lal, W.-S. Chang, S. Link, and P. Nordlander, "Plasmons in strongly coupled metallic nanostructures," Chem. Rev. **111**(6), 3913–3961 (2011).
49. R. A. Chipman, "Depolarization index and the average degree of polarization," Appl. Opt. **44**(13), 2490–2495 (2005).
50. N. Berova, K. Nakanishi, R. W. Woody, and R. Woody, *Circular dichroism: Principles and applications* (John Wiley & Sons, 2000).